Radiation-damage investigation of a DNA 16-mer

Valéria Bugris,[a,b] Veronika Harmat,[a,c] Györgyi Ferenc,[d] Sándor Brockhauser,[a,e] Ian Carmichael[f] and Elspeth F. Garman[b]*

[a]X-ray Crystallography Laboratory, Biological Research Centre, HAC-BRC, Temesvári krt. 62, Szeged 6726, Hungary, [b]Department of Biochemistry, University of Oxford, South Parks Road, Oxford OX1 3QU, UK, [c]Laboratory of Structural Chemistry and Biology and MTA–ELTE Protein Modeling Research Group, Eötvös Loránd University, Budapest, Hungary, [d]Nucleic Acid Synthesis Laboratory, Biological Research Centre, HAC-BRC, Temesvári krt. 62, Szeged 6726, Hungary, [e]European X-ray Free-Electron Laser Facility GmbH (EuXFEL), Holzkoppel 4, 22869 Schenefeld, Germany, and [f]Notre Dame Radiation Laboratory, University of Notre Dame, Notre Dame, IN 46556, USA. *Correspondence e-mail: elspeth.garman@bioch.ox.ac.uk

In macromolecular crystallography, a great deal of effort has been invested in understanding radiation-damage progression. While the sensitivity of protein crystals has been well characterized, crystals of DNA and of DNA–protein complexes have not thus far been studied as thoroughly. Here, a systematic investigation of radiation damage to a crystal of a DNA 16-mer diffracting to 1.8 Å resolution and held at 100 K, up to an absorbed dose of 45 MGy, is reported. The RIDL (Radiation-Induced Density Loss) automated computational tool was used for electron-density analysis. Both the global and specific damage to the DNA crystal as a function of dose were monitored, following careful calibration of the X-ray flux and beam profile. The DNA crystal was found to be fairly radiation insensitive to both global and specific damage, with half of the initial diffraction intensity being lost at an absorbed average diffraction-weighted dose, $D_{1/2}$, of 19 MGy, compared with 9 MGy for chicken egg-white lysozyme crystals under the same beam conditions but at the higher resolution of 1.4 Å. The coefficient of sensitivity of the DNA crystal was 0.014 $\text{Å}^2\,\text{MGy}^{-1}$, which is similar to that observed for proteins. These results imply that the significantly greater radiation hardness of DNA and RNA compared with protein observed in a DNA–protein complex and an RNA–protein complex could be due to scavenging action by the protein, thereby protecting the DNA and RNA in these studies. In terms of specific damage, the regions of DNA that were found to be sensitive were those associated with some of the bound calcium ions sequestered from the crystallization buffer. In contrast, moieties farther from these sites showed only small changes even at higher doses.
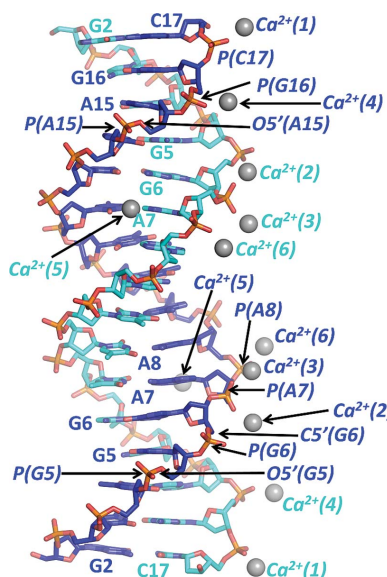
1. Introduction

X-ray crystallography gives a space- and time-averaged structure of a macromolecule. It is currently the major technique used to solve such structures to near-atomic-level resolution (ångström resolution). By solving the structure of the macromolecules/complexes of interest, an understanding of the likely modes of action can be gained and questions about their function can be answered. In order to be able to provide detailed explanations for the function, reaction mechanism or interactions in question, excellent structure quality is needed. Thus, crystallographic method development allowing accurate structure determination is vital.

A major limitation of X-ray crystallography is that the majority of absorbed X-rays (rather than the elastically scattered minority which provide the desired diffraction pattern) damage the fragile macromolecular crystals, which can hinder structure determination or result in flawed biolo-

gical interpretations [for example for bacteriorhodopsin (Matsui *et al.*, 2002) and xylose isomerase (Taberman *et al.*, 2019); for a review, see Garman & Weik (2017)].

Radiation damage to the sample is caused by the absorption of photons from the beam either via the photoelectric effect (total absorption of the photon followed by the ejection of an inner shell electron and the subsequent emission of an Auger electron or fluorescent X-ray depending on the atomic number of the affected atom) or via momentum transfer through Compton scattering (inelastic scattering of the photon, which then escapes following a varying amount of energy loss to an atomic electron, which may also be ejected). At the incident X-ray energies (E_{inc}) normally used in macromolecular crystallography (MX), the photoelectric effect has a much higher cross-section and dominates the interaction, at E_{inc} = 12.4 keV accounting for over 90% (for a 100 μm-thick non-metal-containing crystal) of the energy deposited by the beam (Garman, 2010). Typically, each released photoelectron has enough energy to induce up to 500 further ionizations, which in turn can result in the formation of radical species throughout the crystal. In macromolecular crystals, the presence of 20–80% solvent makes the radiolysis of this fraction a major contributor to the subsequent creation of these potentially deleterious species (O'Neill *et al.*, 2002). Some of the energy deposited by the beam during these processes is converted into heat, which may induce a temperature rise in the sample (Snell *et al.*, 2007; Warren *et al.*, 2019). The diffracted photons, in contrast, are scattered elastically and thus do not contribute to the damage.

A wide literature has accumulated which addresses various aspects of radiation-damage progression, and highlights the reasons why crystallographers should be aware of this issue and adopt methods to minimize its effects (Garman & Owen, 2006; Ravelli & Garman, 2006; Holton, 2009). Radiation-damage effects are usually separated into two categories based on their different characteristics. Global damage is observed in reciprocal space in the diffraction pattern often as an overall loss of reflection intensities, a loss of resolution, unit-cell volume expansion and usually increasing mosaicity. These phenomena have been well characterized and dose limits have been suggested, such as the experimental dose limit (determined for data to 2.2 Å resolution) of 30 MGy [1 Gy (gray) = 1 J kg^{-1}; energy absorbed/mass] at 100 K (subsequently denoted cryo-) beyond which data are likely to be compromised (Owen *et al.*, 2006; Nave & Garman, 2005). In general, for cryo-cooled protein crystals every additional absorbed dose increment of approximately 10 MGy results in a loss of about 1 Å resolution in the diffraction pattern and thus also in the final structure (Howells *et al.*, 2009).

Specific damage involves radiation-induced chemical and conformational changes in macromolecular structures (Helliwell, 1988). It is observed to occur in a reproducible order in protein crystals: first metallo-centres are reduced and disulfide bonds are cleaved, followed by the decarboxylation of acidic residues and then methionine C—S bond cleavage (Ravelli & McSweeney, 2000; Weik *et al.*, 2000; Burmeister, 2000). Previously, an additional manifestation of specific damage had

been suggested to be –OH cleavage from tyrosine residues (Burmeister, 2000). However, it was subsequently shown that the observed electron-density loss round this –OH group was instead due to movement of the entire tyrosine ring (Bury *et al.*, 2017).

Crystallographic investigations of X-ray radiation-induced changes in MX to nucleic acid crystals themselves and the larger class of nucleoprotein complexes are generally less comprehensive, and a specific damage 'pecking order' for them has not yet been established. Nucleic acid and nucleoprotein complexes now (as of 6 February 2019; https://www.rcsb.org/stats/summary) comprise approximately 6.34% of MX-derived structures deposited within the Protein Data Bank (PDB). While systematic radiation-damage studies on crystals of an RNA–protein complex (Bury, McGeehan *et al.*, 2016) and a DNA–protein complex (Bury *et al.*, 2015) have already been reported in detail, to our knowledge no comparable investigations have been performed on crystals containing only DNA, which would allow a direct comparison with previous work.

The impact of ionizing radiation on DNA has been investigated under a wide variety of experimental conditions. Among the most relevant to the present study are those conducted in glassy matrices at 77 K, involving the search, by electron paramagnetic resonance spectroscopy, for the radical species that are eventually formed following the initial ionization and excitation events (Becker & Sevilla, 1993; Becker *et al.*, 2007). X-ray damage has also been observed during the course of X-ray photoelectron spectroscopic (XPS) investigations of nucleic acids deposited on a surface under vacuum (Ptasińska & Sanche, 2007), and the nature of some of the damage sites could be determined directly from the measured XPS signals. Efforts to probe the direct effect of low-energy-electron interactions by dissociative electron attachment to isolated, immobilized DNA molecules on surfaces under vacuum conditions (Boudaïffa *et al.*, 2000) are also of importance and results have been reviewed more recently (Alizadeh & Sanche, 2014; Alizadeh *et al.*, 2015). However, solution-phase studies have tended to focus on the consequences of hydroxyl radical attack in aqueous room-temperature media (Michael & O'Neill, 2000; Cadet *et al.*, 1999; Spotheim-Maurizot & Davídková, 2011). While no doubt biologically relevant, the effects of this particular reactive species are of less interest here since hydroxyl radicals are assumed to be immobile at 100 K (Owen *et al.*, 2012), the temperature used for the study reported here. Cellular DNA, which is mainly in the B form (base pairs perpendicular to the helix axis), has around 20 water molecules per nucleotide in the first two hydration layers, and this drastically modifies the yield of base lesions when DNA is damaged at both low temperature and room temperature (Yokoya *et al.*, 2002). Note that in the DNA literature, holes produced by ionization events in this hydration layer are incorporated into the classification as direct damage, with the hole being thought to transfer promptly to the DNA (Swarts *et al.*, 2007).

Double-brominated DNA crystals have been probed using Raman micro-spectroscopy, showing radiation-damage-

induced changes. The researchers identified breakages of a single carbon–bromine covalent bond by both MX and Raman techniques and potentially other damage to DNA, but they were not able to completely assign all of the signals (McGeehan *et al.*, 2007). A better appreciation of the mechanisms involved may eventually allow the manipulation of the effects of ionizing radiation at the molecular level (McGeehan *et al.*, 2007).

Structural studies on DNA and RNA and complexes with proteins have been widely reported (Berman *et al.*, 2000), with over 10 000 entries now in the PDB: 78.6% of these were solved by MX, of which 86% were at cryo-temperatures. However, as noted above, no systematic radiation-damage MX investigation has been published which shows specific changes within the native DNA and/or RNA molecule. This may be related to the fact that DNA itself is a relatively stable molecule (Halliwell & Gutteridge, 1998). Radiation chemists and biologists have studied DNA in solution because it is the macromolecule responsible for the exchange of genetic information, and its stability and radiation resistance have direct consequences for human health (Michael & O'Neill, 2000; Kempner, 1993; Halliwell & Gutteridge, 1998). There is of course a wide range of literature on DNA damage induced by different qualities of ionizing radiation, including studies on the effect of low-linear energy transfer radiations particularly targeted at the biological function of DNA (Kadhim *et al.*, 2006). Although these investigations have uncovered important mechanistic details, a complete picture has yet to emerge.

Using X-ray diffraction data collected at 100 K from a crystal of a protein–RNA complex (TRAP–RNA), the specific damage incidence for both the protein and RNA components (91 kDa amino acids and 53 base pairs, respectively) of a biologically relevant complex over a large dose range (2.07–44.63 MGy) has previously been reported (Bury, McGeehan *et al.*, 2016). The RNA appeared to be far less susceptible to radiation damage than was the protein. Interestingly, the amino acids in contact with RNA suffered lower levels of damage compared with those which were more remote, implying some radioprotection of the protein by the RNA (Bury, McGeehan *et al.*, 2016). Another 100 K study on a crystal of a DNA–protein complex with similar numbers of DNA and protein atoms (382 amino acids, 2496 protein non-H atoms; 35 DNA base pairs, 1429 DNA atoms) again showed greater resistance of the nucleic acid component than the protein to radiation damage (Bury *et al.*, 2015). Together, these results suggest a lower susceptibility of nucleotides than proteins to radiation damage, although the possibility that the nucleotides are protected by the protein cannot be excluded.

In the systematic study that we report here, our objective was to investigate the specific and global radiation-damage mechanisms in DNA crystals harbouring no protein component. By collecting a dose series from a crystal of a DNA 16-mer, we have characterized the specific damage by using an automated tool called *RIDL* (*Radiation-Induced Density Loss*) to analyse the electron-density loss (Bury & Garman, 2018). *RIDL* has been developed to enable the objective detection and quantification of radiation-induced site-specific changes to macromolecular structures as a function of absorbed dose. The program has been designed to extract suitable per-atom descriptors of radiation damage, based on the changes detectable in the structure-factor $F_{\text{obs},n} - F_{\text{obs},1}$ Fourier difference maps through successive dose data sets (numbered 1 to n). The metrics derived using *RIDL* (Bury & Garman, 2018), a computer program that is described below, previously enabled this comparative analysis of specific radiation damage in disparate systems (Bury, Carmichael *et al.*, 2016).

Here, a comprehensive analysis of radiation damage to the 16-mer DNA crystal is presented, including results for the diffraction intensity decay, unit-cell volume expansion and relative isotropic *B*-factor increase with dose, as well as an analysis of the various sites of specific radiation damage in the DNA and the rise in atomic *B* factors during the experiment.
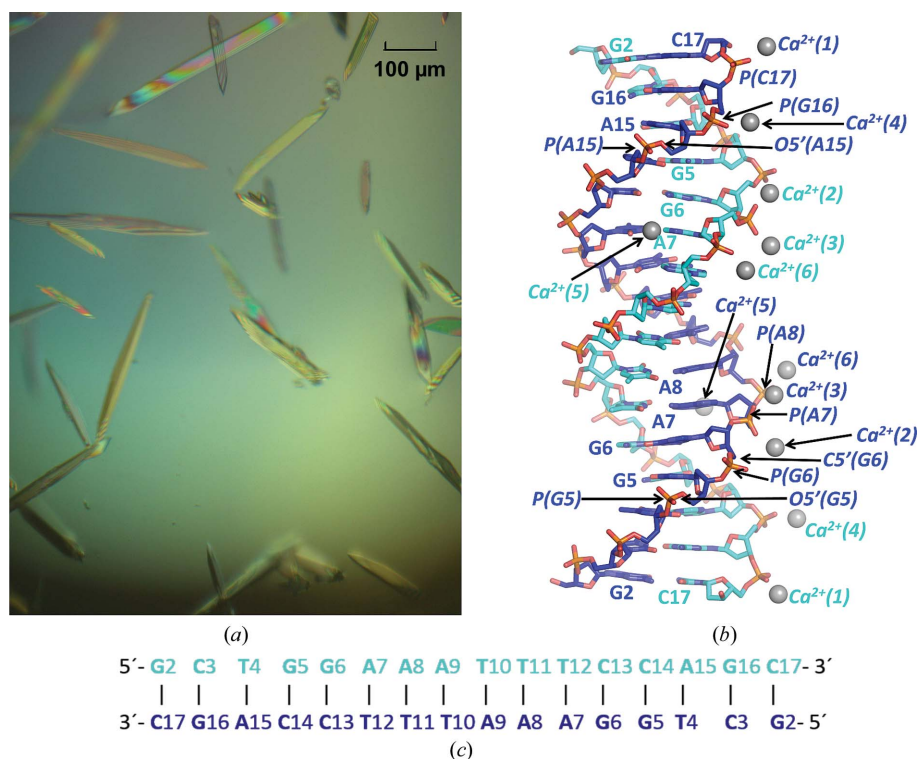
2. Materials and methods

2.1. Synthesis and annealing of DNA duplexes

The 16-mer DNA oligonucleotide was synthesized using a DNA/RNA/LNA H-16 synthesiser (K&A Laborgeraete) by standard β-cyanoethyl phosphoramidite chemistry at a nominal scale of 0.2 µmol. The sequence of the oligonucleotide was 5′-GCTGGAAATTTCCAGC-3′ (G, guanine; C, cytosine; T, thymine; A, adenine). The oligonucleotide was purified by HPLC on an RP-C18 column under ion-pairing conditions [using mobile phases containing 0.1 m*M* triethyl-ammonium acetate (TEAA) pH 6.5 buffer]. The 4,4′-dimethoxytrityl protective group was removed from the 5′-end of the oligonucleotide using 2% TFA on a Poly-Pak column. After lyophilization, the DNA was resuspended in 5 m*M* HEPES pH 6.6 at a concentration of 1.5 m*M*, and the self-complementary strands were annealed by heating to 80°C followed by slow cooling to 25°C. The solution of the DNA duplex was immediately used for crystallization.

2.2. Crystallization

Crystals were grown in a reproducible fashion using the hanging-drop vapour-diffusion method with 2 µl 1.5 m*M* DNA solution (5 m*M* HEPES pH 6.6) plus 2 µl 10 m*M* HEPES pH 6.6 plus 4 µl reservoir solution equilibrated against a reservoir consisting of 1 ml 34% PEG 200, 600 m*M* CaCl$_2$ and 10 m*M* HEPES pH 8.6. The conditions were optimized from those previously reported for the crystallization of the 17-mer DNA sequence containing an extra cytosine at its 5′ end (Huang *et al.*, 2005; PDB entry 1sgs) and the same 16-mer as suggested by McGeehan *et al.* (2007) and Brockhauser *et al.* (2008). Crystals were visible after a day and grew to approximate dimensions of 300 × 35 × 15 µm within 3–5 days (Fig. 1). These DNA crystals were used for data collection at 100 K without added cryoprotectant since the PEG 200 in the crystallization buffer was sufficient for cryoprotection.

5´- **G2 C3 T4 G5 G6 A7 A8 A9 T10 T11 T12 C13 C14 A15 G16 C17**- 3´
| | | | | | | | | | | | | | | |
3´- **C17 G16 A15 C14 C13 T12 T11 T10 A9 A8 A7 G6 G5 T4 C3 G2**- 5´

(c)

Figure 1
(a) The 16-mer DNA crystals and (b) the final structure of the double helix of the DNA segment. In (b) atoms are shown as follows: carbon, sky blue and blue for different DNA chains; phosphorus, orange; oxygen, red; nitrogen, dark blue. Nucleotides are labelled G, A, T and C and individual atoms are labelled in italics, with the nucleotide ID in parentheses. $Ca^{2+}(1)$, $Ca^{2+}(2)$ and $Ca^{2+}(3)$ all lie on a vertical threefold axis and have 1/3 occupancy each. (c) The 2D structure of the duplex of the DNA 16-mer [note that the numbering is as used in Huang *et al.* (2005) so that the sequence starts at nucleotide 2].

2.3. Beam calibration

Data were collected on beamline I24 at Diamond Light Source (DLS). Before data collection, the X-ray flux and beam profile were calibrated as described below to enable the recovery of accurate information for the dose calculations.

To determine the beam flux (the number of photons per unit time) a diode linked to a picoammeter was used, as described previously (Owen *et al.*, 2009). The 500 μm-thick silicon PIN diode (Canberra, model No. PD300-500CB) was placed at the crystal position and the diode current was measured and converted into photons s^{-1} using the appropriate pre-determined relationship.

A calibrated metal edge and the same silicon pin diode were used to profile the horizontal and vertical beam profiles. The edge was moved through the beam in order to obscure increasing amounts of the beam, and the current produced by the remaining X-rays was recorded after each move. Data collected in both directions (vertical and horizontal) were plotted and the full widths at half-maximum (FWHM) were calculated using a DLS beamline software utility which took the derivative of the edge-scan measurements. The beam had an approximately 'top-hat' profile with an FWHM of 52.7 μm in the horizontal direction and a 50 μm FWHM Gaussian shape in the vertical plane (Fig. 2).

2.4. Data collection

Data were collected at 100 K using a wavelength of 0.9686 Å (12.8 keV) and a PILATUS3 6M detector at a crystal-to-detector distance that gave a resolution of 2 Å at the largest inscribed circle on the detector face. 48 complete data sets were collected from one position of the DNA crystal (35 × 279 × 15 μm) using identical experimental protocols. The flux was 3.52×10^{11} photons s^{-1} (at 10% transmission).

From the DNA crystal (space group *H*32), four successive runs of 12 data sets (one run = 720° rotation, one data set = 60°) were collected (oscillation of 0.1°/image with 10% beam transmission and an exposure time of 0.02 s). The maximum resolution obtained was 1.8 Å (Table 1).

Radiation-damage data-set series were also collected under identical beam conditions from two native chicken egg-white lysozyme crystals as a cross-check on the dose estimates and beam calibrations, since the resolution-dependent intensity decay of lysozyme at 100 K has been previously characterized by a number of research groups. The doses to reduce the initial diffraction intensity to half for various resolution shells (Teng & Moffat, 2000) and for the total diffraction intensity to fall to half of its initial value (see, for example, Teng & Moffat, 2002; de la Mora *et al.*, 2011) at various resolutions have both been determined.
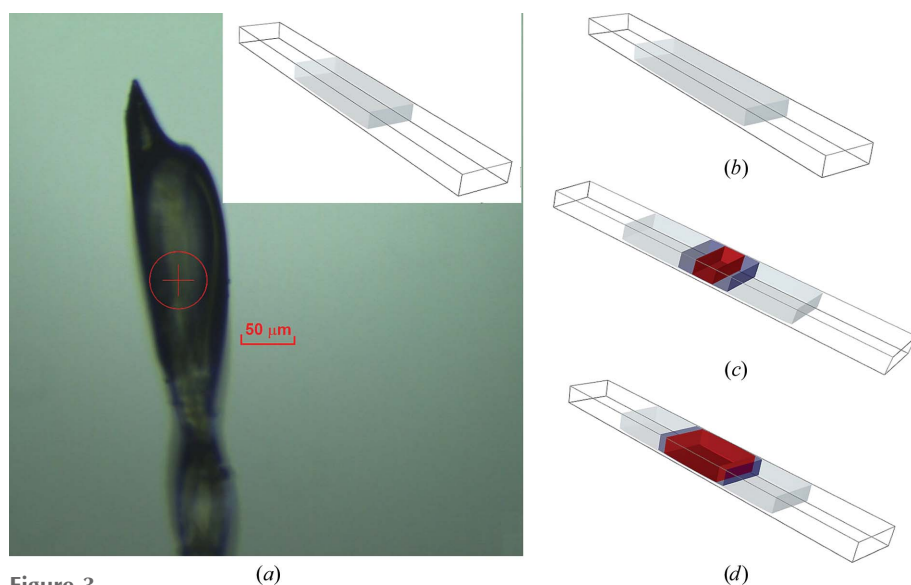
2.5. Dose calculation

In order to reliably interpret the X-ray radiation-damage data, it is important to have an accurate estimate of the absorbed X-ray dose. *RADDOSE*-3D (Zeldin, Gerstel *et al.*, 2013) was used to calculate the dose distributions after the first [Fig. 3(a)], the 12th [Fig. 3(b)], the 24th [Fig. 3(c)] and the 48th [Fig. 3(d)] data sets, so that the progression of damage events could be associated with the corresponding dose differences.

The beam-intensity profiles (Fig. 2) were found to be approximately top-hat (horizontally) and Gaussian (vertically), but *RADDOSE*-3D allows either top-hat in both directions or Gaussian in both directions (as well as taking a 2D experimentally measured profile if available). Thus, the beam was modelled horizontally as a very broad 1000 μm FWHM Gaussian which was collimated to 52.7 μm and as a 50.0 μm uncollimated (1000 μm collimation aperture used) Gaussian in the vertical direction. The photon flux prior to beam attenuation was measured as 3.52×10^{12} photons s^{-1} and was constant throughout the experiment. The calculation of the crystal absorption coefficients in *RADDOSE*-3D
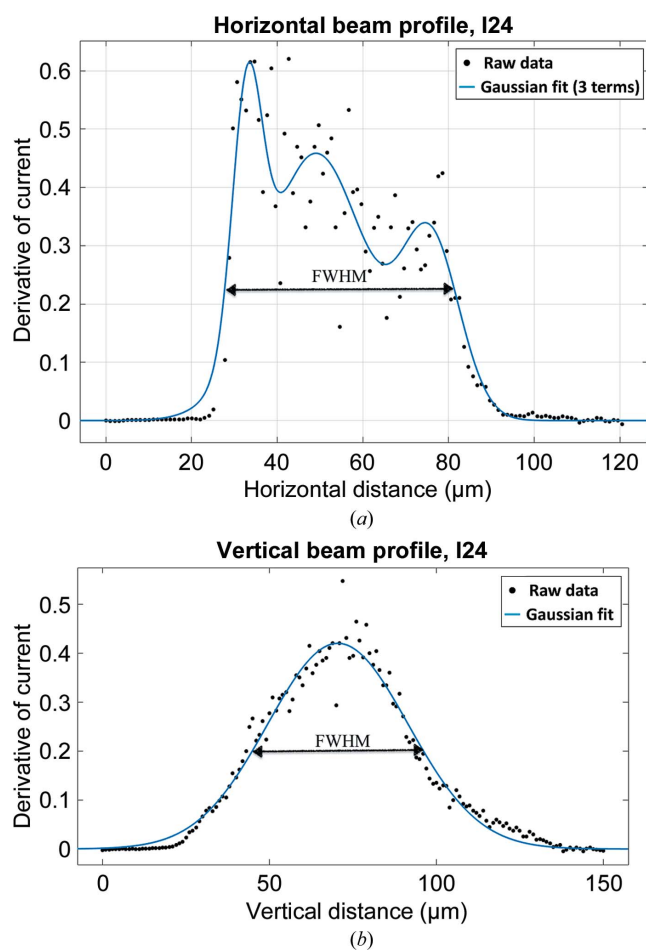
Figure 2
Beam-profile calibration on the I24 beamline at DLS. The FWHMs of the beam profiles are shown: (*a*) 52.7 µm approximately top-hat profile horizontally and (*b*) 50.0 µm Gaussian vertically.

Figure 3
(*a*) The DNA crystal within the loop during data collection. The inset in (*a*), (*b*), (*c*) and (*d*) are online *RADDOSE*-3D (Zeldin *et al.*, 2013) calculations of dose distributions in the cuboid-shaped crystal after the (*a*, inset) first (DWD: 0.48 MGy), (*b*) 12th (12.0 MGy), (*c*) 24th (23.5 MGy) and (*d*) 48th (45.5 MGy) data sets. The dose isosurfaces are drawn at 0.1 MGy (white), 20 MGy (blue) and 30 MGy (dark red).

included the water and the heavy-atom content from the crystallization conditions (the sulfur from the HEPES buffer and the calcium and chlorine from the $CaCl_2$). All of the results on radiation-damage progression were plotted against the resulting average diffraction-weighted dose (DWD; Zeldin, Brockhauser *et al.*, 2013) values (the average DWD for each data set is added to the cumulative total dose for each preceding data set to obtain the dose at that point in the experiment).

2.6. Data processing

Diffraction data were processed with *DIALS* (Sauter *et al.*, 2013; Winter *et al.*, 2018) and the *CCP*4 package (Winn *et al.*, 2011) using *CCP4i*2 (Potterton *et al.*, 2018), including *AIMLESS* (Evans & Murshudov, 2013) and *POINTLESS* (Evans, 2006). The first data set (low-dose data set) from the crystal was used to obtain phases by molecular replacement (MR) in *Phaser* (McCoy *et al.*, 2007), using the structure containing one extra nucleotide (Huang *et al.*, 2005; McGeehan *et al.*, 2007; PDB entry 1sgs) as the search model. Note that as a result of using this MR model and to avoid confusion, we have retained the same nucleotide numbering in the 16-mer studied here, so that it starts at G2 and ends at C17. The structure was refined in *REFMAC*5 (Murshudov *et al.*, 2011) using TLS and restrained refinement, with the DNA segment as a single TLS group. Individual atomic *B* factors were refined and 5% of the reflections were withheld for use in R_{free}. Manual model building was carried out using *Coot* (Emsley *et al.*, 2010).

The final model contains 16 nucleotide residues and 38 water molecules (two of them in alternate positions) as well as six Ca^{2+} ion positions {three fully occupied sites [Ca^{2+}(4) to Ca^{2+}(6)] with an additional three Ca^{2+} ions sitting on a crystallographic three-fold axis each with 1/3 occupancy [Ca^{2+}(1) to Ca^{2+}(3)], giving a total of four calcium ions per DNA monomer for the dose calculations}. The DNA double helix is created by crystallographic twofold rotation. To create models from the higher-dose data sets (dose greater than the first data set), the final model from the first data set was used and further refined using *REFMAC*5 against the structure factors output by *AIMLESS* for the higher-dose data sets (restrained coordinate and individual *B*-factor refinement, with H atoms generated). The structures refined against data sets with absorbed doses of 0.48, 6.2, 12.0, 17.7, 23.5 and 29.2 MGy have been deposited in the PDB as entries 6qt1, 6qt2, 6qt3, 6qt4, 6qt5 and 6qt6, respectively. For the analyses, the resolution cutoff for all data sets was 1.8 Å. However, the esti-

Table 1
Crystallographic data-collection, processing and structure-refinement statistics for the DNA crystal at 100 K in space group $H32$.

Data were collected on beamline I24 at Diamond Light Source (λ = 0.9686 Å; incident flux 3.52×10^{11} photons s^{-1}). The data-collection protocol involved eight full 360° rotations of the crystal. Each full rotation was divided into six wedges of 60° each, resulting in 48 data sets (the exposure time for each data set was 12 s). Structures were refined against data sets processed to 1.8 Å resolution. Values in parentheses are for the outer resolution shell.

Data set	1	7	13	19	25	31
PDB code	6qt1	6qt2	6qt3	6qt4	6qt5	6qt6
Data collection						
Cumulative dose (average DWD) (MGy)	0.48	6.2	12.0	17.7	23.5	29.2
Data processing						
Unit-cell parameters						
$a = b$ (Å)	36.82	36.86	36.89	36.93	36.93	36.97
c (Å)	161.93	162.06	162.20	162.36	162.48	162.57
Resolution (Å)	31.31–1.80 (1.85–1.80)	31.34–1.80 (1.85–1.80)	31.36–1.80 (1.85–1.80)	31.40–1.80 (1.85–1.80)	31.40–1.80 (1.85–1.80)	31.43–1.80 (1.85–1.80)
$\langle I/\sigma(I)\rangle$	9.4 (1.0)	8.7 (0.9)	5.4 (0.3)	3.5 (0.2)	2.6 (0.1)	1.8 (0.0)
Completeness (%)	92.1 (59.0)	92.5 (60.0)	92.1 (56.4)	92.2 (56.7)	92.2 (57.5)	92.3 (57.7)
Multiplicity	2.9 (2.5)	3.0 (2.5)	2.9 (2.5)	3.0 (2.5)	2.9 (2.6)	3.0 (2.6)
R_{meas}	0.053 (0.959)	0.068 (1.288)	0.072 (3.470)	0.099 (5.447)	0.127 (16.7)	0.167 (143)
$CC_{1/2}$	0.998 (0.608)	0.996 (0.318)	0.997 (0.153)	0.995 (0.237)	0.992 (0.190)	0.983 (0.0)
Normalized intensity†	1	0.93	0.798	0.69	0.57	0.47
Wilson B (Å^2)	36.58	38.17	40.91	51.31	60.97	68.11
Estimated resolution limit‡ (Å)	1.80	1.80	1.89	1.97	2.17	2.30
Refinement and model quality§						
R/R_{free}	0.220/0.256	0.220/0.282	0.222/0.291	0.232/0.310	0.248/0.345	0.270/0.369
Mean atomic B factor (Å^2)	49.35	50.01	52.57	55.10	57.18	57.75
R.m.s.d., bond lengths (Å)	0.011	0.0096	0.0087	0.0085	0.0074	0.0070
R.m.s.d., bond angles (°)	1.914	1.764	1.670	1.710	1.567	1.540

† I_n/I_1, where I_n is the weighted average of the average intensities of the resolution shells of a complete data set for dose level n. ‡ Resolution limit estimated from $CC_{1/2} > 0.30$ as calculated by *AIMLESS*. (The resolution cutoff for data analysis and structure refinement was set to 1.8 Å for all data sets.) § The final model derived from the lowest dose data set was further refined against the later data sets. No. of atoms in the final model: DNA, 325; Ca^{2+}, 4; water, 38. Note that there are six calcium-ion positions, three at full occupancy and three at 1/3 occupancy.

mated resolution of the data sets decreases with dose (Table 1, where the resolution limits are estimated using $CC_{1/2} > 0.30$). The 35.0 MGy structure was of such poor refined quality (R and R_{free} = 0.40 and 0.46, respectively) owing to the degradation of the diffraction and low signal to noise at higher resolution in data set 37 that it has not been deposited. Figures showing the structure and electron-density maps were created and drawn using *PyMOL* (Schrödinger).

2.7. Specific damage analysis

As noted above, to simplify the search for specific damage events we used *RIDL* (Bury & Garman, 2018). This program calculates per-atom metrics to describe the electron-density changes between complete diffraction data sets collected at successive doses. These data allow the location and frequency of specific damage sites to be investigated on a range of scales from nucleotides to specific atoms, since the cleavage of chemical bonds and disordering of atoms typically leaves a signature of electron-density loss in $F_{\text{obs},n} - F_{\text{obs},1}$ difference maps. These are captured in the present work by the $D_{\text{neg}}(\text{atom})$ metric distribution over all atoms present for every sixth data set. This provides a suitable description of the overall magnitude of electron density lost at an atomic site and is defined as

$$D_{\text{neg}}(\text{atom}) = \frac{\sum\limits_{\nu \in V_{\text{atom}}^{-}} -\rho_{\Delta}(\nu) \cdot \rho_{\text{calc}}(\nu)}{\sum\limits_{\nu \in V_{\text{atom}}^{-}} \rho_{\text{calc}}(\nu)}, \quad (1)$$

where $\rho_{\Delta}(\nu)$ is the difference density map, $F_{\text{obs},n} - F_{\text{obs},1}$, and $\rho_{\text{calc}}(\nu)$ is the electron-density map calculated using F_{calc} amplitudes and φ_{calc} phases of the refined model at a voxel ν within the volume pertaining to that atom, V_{atom}. This metric is the weighted average of the electron-density loss over all voxels V_{atom}^{-} in the vicinity of that atom which have negative values in the difference density map $[\rho_{\Delta}(\nu) < 0]$.

3. Results

A cuboid-shaped crystal was used for data collection [Fig. 3(a)] and belonged to space group $H32$. Similarly to the original structure, which included one additional nucleotide (Huang *et al.*, 2005; McGeehan *et al.*, 2007), each asymmetric unit contained a single DNA strand, which is half of the DNA double strand, and the unit cell thus contained 18 monomers. The crystal had a solvent content of 41%.

To monitor the global damage, I_n/I_1 was plotted as a function of dose, where I_n is the weighted average of the average intensities of the resolution shells of a complete data set for dose level n and is calculated from the *AIMLESS*-output intensities as (Bury, McGeehan *et al.*, 2016)

$$I_n = \frac{\sum\limits_{i=1}^{N_{\text{res}}} \text{Av} \, I_{(i)} \cdot N_{\text{meas}(i)}}{\sum\limits_{i=1}^{N_{\text{res}}} N_{\text{meas}(i)}}, \quad (2)$$

where N_{res} is the number of resolution shells in the diffraction pattern, $N_{meas(i)}$ is the number of observed reflections for resolution shell $i \in \{1, \ldots, N_{res}\}$ and $Av I_{(i)}$ is the average intensity for resolution shell i. The normalized intensity I_n/I_1 is plotted against the average DWD (Fig. 4). Due to the data-collection strategy and scaling protocol, the same $60°$ wedge of the crystal was irradiated during every sixth data set. Owing to the anisotropic intensity profile and the shape of the beam, irradiating a crystal smaller than the beam resulted in different volumes of the crystal being exposed to the most intense part of the beam for each of these wedges. This caused differences in mean intensities between the sequential data sets for which scaling could not compensate. As shown in Fig. 4(a), the mean intensity decay relative to the first data set shows an oscillatory behaviour. To allow the comparison of similar volume wedges, Fig. 4(b) shows the mean intensities normalized to the mean of the first data set for the same crystal rotation wedge,
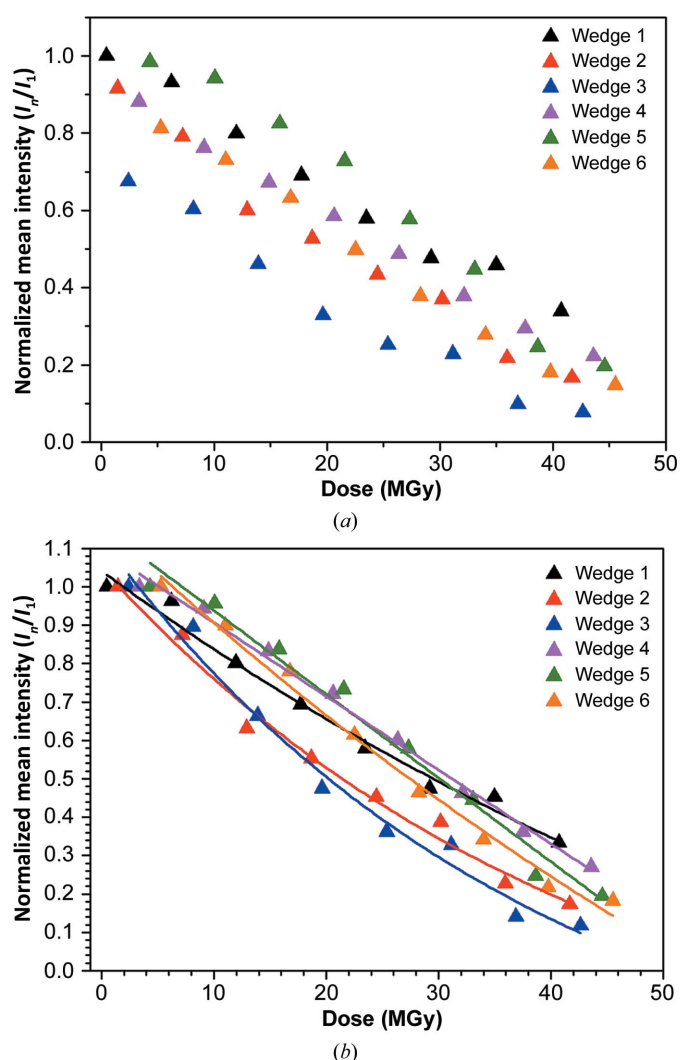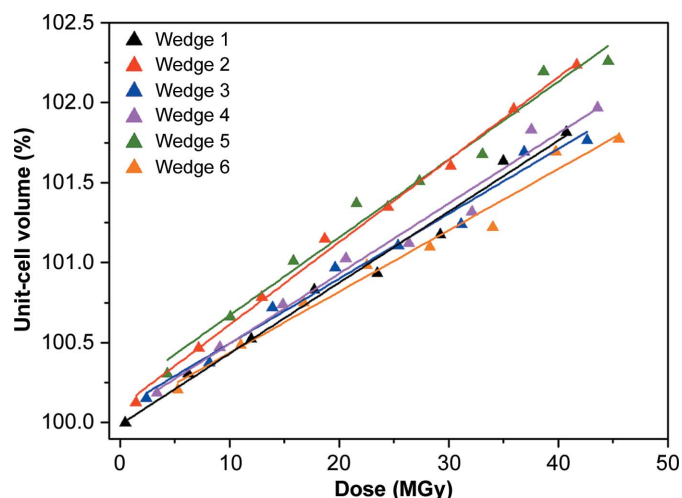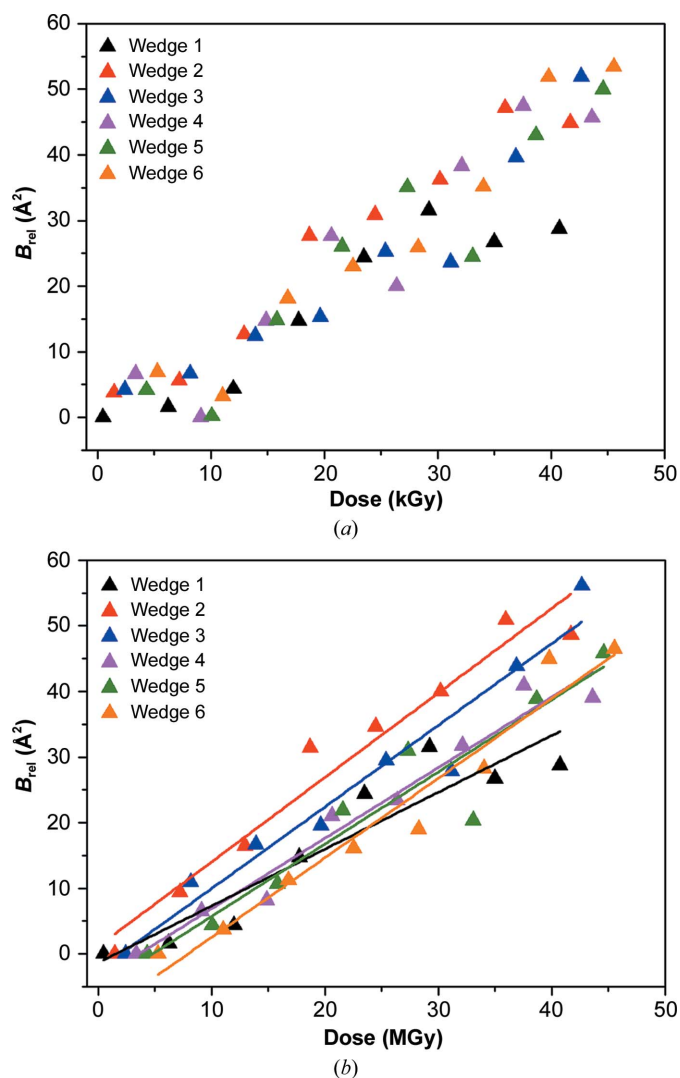

Figure 5
Unit-cell expansion of the DNA crystal. A linear increase with a similar gradient is observed for all rotation wedges over the whole dose range.

using data sets 1–6 to normalize the later data sets. The fits shown are exponentials, which all have R^2 values of >0.97. Averaging all of the resulting gradients results in a $D_{1/2}$ of 18.9 ($\pm$2.6) MGy for all data to 1.8 Å resolution. The two native lysozyme crystals irradiated as controls gave an average $D_{1/2}$ of 9.1 MGy (data not shown) for all data to 1.4 Å resolution.

Unit-cell expansion can also be detected for the DNA 16-mer crystal and it continues to increase linearly up to the highest dose measured (45.5 MGy; Fig. 5), in contrast to some previous results for protein crystals in which the increase was linear at low dose but then plateaued at higher doses [see, for example, Fig. 1(b) in Garman (2010) for holoferritin crystals above 30 MGy]. There is a loss of diffraction resolution from 1.8 to 1.96 Å starting at the 14th data set (above 12.5 MGy) and falling to 2.6 Å at 35.0 MGy. In addition, R_{meas} increases from the 14th data set onwards.

Another common metric used to monitor radiation damage at 100 K is the relative isotropic B factor (B_{rel}), which is linearly dependent on dose (Kmetko *et al.*, 2006). This is defined as the difference in Wilson B factor between the nth data set and the first data set ($B_{rel} = B_n - B_1$), and its behaviour with dose is shown in Figs. 6(a) and 6(b), where the normalization is as in Fig. 4. Fig. 6(a) shows $B_{rel} = B_n - B_1$ calculated for the 48 data sets and Fig. 6(b) presents B_{rel} for the six wedges separated [*i.e.* $B_{rel} = B_{(6m+i)} - B_i$, where m is 0–7 and i is 1–6] normalized to the mean of the first data set of the same crystal rotation wedge, using data sets 1–6 to normalize the later data sets. The relative B factors can be interpreted as being proportional to the change in the mean-squared atomic displacements. Since in our case the I_n/I_1, the unit-cell volume and B_{rel} metrics all showed a dependence on the particular crystal rotation wedge, for analysing specific radiation damage the results from only the first wedge are discussed in detail.

$F_{obs,n} - F_{obs,1}$ difference electron densities were compared and analysed for data sets n = 7, 13, 19, 25, 31 and 37 (wedge i = 1 data sets) to characterize specific radiation damage

Figure 4
Mean intensity decay for the 48 DNA data sets (a) normalized to the mean for the first data set and (b) normalized to the mean of the first data set of the same crystal rotation wedge using data sets 1–6 to normalize the later data sets. The fits shown are exponentials, which all have R^2 values of >0.97.

Figure 6
Relative isotropic B factor for the DNA crystal. A linear increase is observed with increasing dose over the reported dose range. $B_{rel} = B_n - B_1$ calculated (a) for the 48 data sets and (b) for the six wedges separated [$i.e.$ $B_{rel} = B_{(6m + i)} - B_i$, where m is 0–7 and i is 1–6] and normalized to the mean of the first data set of the same crystal rotation wedge, using data sets 1–6 to normalize the later data sets.

indicated by local electron-density changes (Fig. 7). For the refined models created from the higher-dose data sets ($i.e.$ a dose greater than the first data set), the resolution of the electron-density map decreased, and Fourier ripples appeared around calcium ions sitting on the crystallographic threefold axis. The largest changes in electron density are at and around some of the calcium ions [$Ca^{2+}(1)$, $Ca^{2+}(2)$, $Ca^{2+}(3)$ and $Ca^{2+}(4)$, as depicted in Fig. 1(b)] and some of the phosphate moieties (those of the fifth, sixth and 14th–17th nucleotide residues), all of which are involved in the water-mediated hydrogen-bond network (Supplementary Fig. S1). At higher doses, smaller electron-density changes were observed at the heterocyclic moieties. In contrast, nucleotide residues 8–13, which form a more flexible region owing to a lack of any crystallographic contacts, show no significant electron-density changes and neither do similarly located ordered calcium ions, even at very high dose.

Fig. 8 details the distribution of specific damage detected using $RIDL$ throughout the overall structure for every sixth data set. The $RIDL$ D_{neg}(atom) analysis (see Section 2) also shows that the average electron-density change of calcium ions is larger than that of nucleotide atoms (Fig. 8). The D_{neg}(atom) and top damage sites (Fig. 10), both derived from the $F_{obs,n} - F_{obs,1}$ maps, show that there are differences in the rates of electron-density change amongst the six calcium ions and their environments. At a dose of 6.2 MGy only $Ca^{2+}(1)$ is damaged (it is apparently reduced since the electron-density changes are positive as shown in Supplementary Fig. S2), while at 12.0 MGy this and the other two calcium ions sitting on the threefold axis [$Ca^{2+}(2)$ and $Ca^{2+}(3)$] also show significant electron-density changes ($>\pm3\sigma$). Smaller changes are seen in the vicinity of $Ca^{2+}(4)$ above 12 MGy, and $Ca^{2+}(5)$ and $Ca^{2+}(6)$ show only minor changes across the whole dose range (Supplementary Fig. S2).

$RIDL$ additionally flags up damage sites in the vicinity of the phosphorus–oxygen and oxygen–sugar bonds (see Fig. 7). The guanine moieties are slightly more damaged than the other three nucleotides, as is also observed in EPR experiments (Becker $et~al.$, 2007), and thymine shows the least density loss. All four nucleotide types suffered radiation damage at fairly similar rates, differences becoming particularly noticeable at the higher doses (>24 MGy). It should be noted, however, that in this small oligonucleotide there are only four nucleotides of each type. Thus, the average characteristics found here could easily be distorted by local interactions specific to this structure. Fig. 9 shows the normalized frequencies of D_{neg}(atom) values.

Analysis of the electron loss per $Å^{-3}$ with respect to absorbed dose was performed for different components of the structure (nucleotide types, calcium ions and water molecules). The distribution of the top 25 sites at different positions within the structure is shown in Fig. 10 along with the relative change in electron densities (see Supplementary Table S1 for lists of the top 25 sites as a function of dose). At higher dose values these sites are more concentrated at the two ends of the DNA chain, particularly in the vicinity of the correspondingly located calcium ions. In Fig. 11, the key indicates the nearest atom in the DNA to which specific damage has been assigned. It is evident that clear differential specific damage rates are present not only between different nucleotide types but also within a given nucleotide ($e.g.$ guanines in Fig. 10). The top ten electron-loss sites presented in Fig. 11 are all in proximity or directly bound to Ca^{2+} ions [the P atoms of nucleotides 7, 8, 15, 16 and 17, respectively; see Figs. 1(b), 1(c) and 10 for the positions of Ca^{2+} ions along the nucleotide chain], suggesting that complexed metals of larger atomic number may enhance sensitivity to radiation-induced specific damage in this case (see also Supplementary Table S2). $F_{obs,n} - F_{obs,1}$ electron-density maps indicate the breakage of several P—O bonds and relatively few other changes. For instance, there are small levels of electron-density loss at the aromatic groups and at C—O bonds (Fig. 7) at high doses. In contrast to the outer region of the oligonucleotide, the region between nucleotides 9–14 is neither bridged to (ordered)
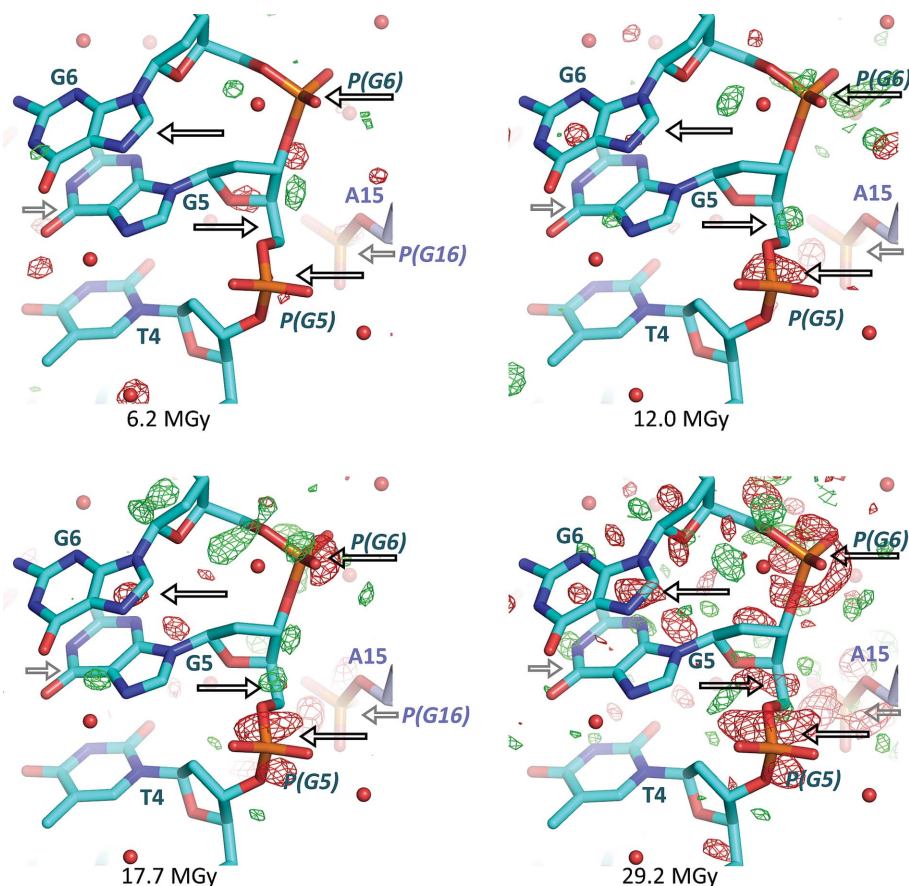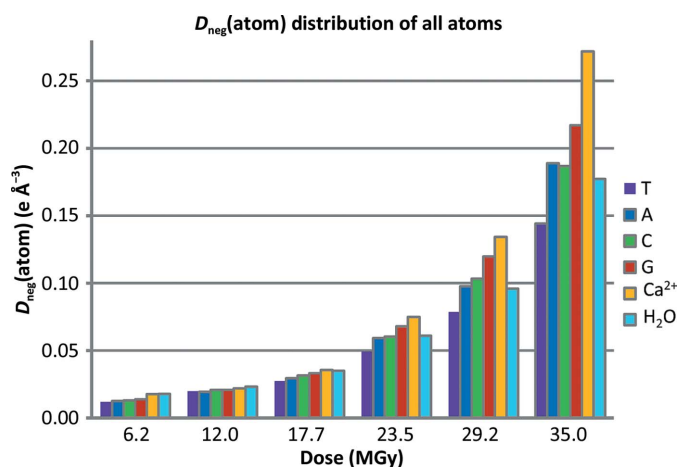
Figure 7
Difference electron-density maps calculated by FFT through the *RIDL* pipeline ($F_{obs,n} - F_{obs,1}$-type maps) contoured for the seventh, 13th, 19th and 31st data sets at 3.0σ and -3.0σ levels in green and red, respectively. Electron-density loss around the phosphate moieties of nucleotides G5 and G6 indicates the occurrence of P—O and C—O bond breaks, while the aromatic groups show only minor changes in electron density (arrows). Atoms are shown as follows: carbon, sky blue for the DNA chain; phosphorus, orange; oxygen, red; nitrogen, dark blue. Nucleotides are labelled with one-letter codes. P atoms are labelled in italics.

calcium ions nor establishes inter-molecular contacts with other double helices in the crystal. The metrics described above indicate that this region seems to be less prone to radiation damage.

The rate of damage to the different P atoms in the DNA structure was not uniform, with large variations in the apparent susceptibility. At a dose of 6.2 MGy the $F_{obs,n} - F_{obs,1}$ map shows significant electron-density change ($>\pm3\sigma$) for the P atoms of only three nucleotides (5, 15 and 16), at 12.0 MGy at four nucleotides (5, 7, 15 and 16) and at 17.7 MGy at six nucleotides (5–7 and 15–17). Further P atoms (nucleotides 8, 9 and 11) start to show electron-density changes only at 35.0 MGy, whereas those in nucleotides 3, 4, 10, 12, 13 and 14 show no changes above $\pm3\sigma$ at this dose. Examples of electron-density changes around the P atoms of nucleotides 5, 6 and 16 are shown in Fig. 7.

In a crystal of a protein–oligonucleotide complex (C.Esp1396I protein–DNA) it was shown that DNA has a relatively high resistance to specific damage, since the onset of specific damage was detected at significantly larger dose values than for the protein residues in crystals (Bury *et al.*, 2015). In that study, the normalized frequency of DNA nucleotides involved in specific radiation damage reached 0.2 at a dose of about 35 MGy. In contrast, similar frequency values for susceptible protein
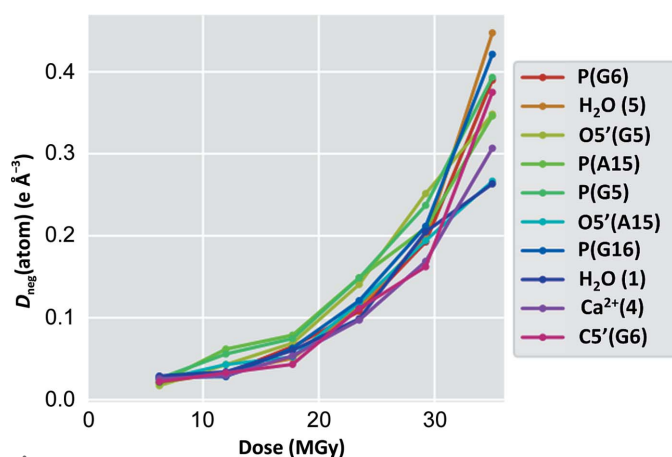

Figure 8
Detected specific damage for each nucleotide type for every sixth data set (data sets 7, 13, 19, 25, 31 and 37). $D_{neg}(atom)$ values averaged for all atoms of each component type indicate the amount of electron-density loss with increasing dose. The oligonucleotides, calcium ions and water molecules are labelled A, C, G, T, Ca^{2+} and H_2O, respectively.
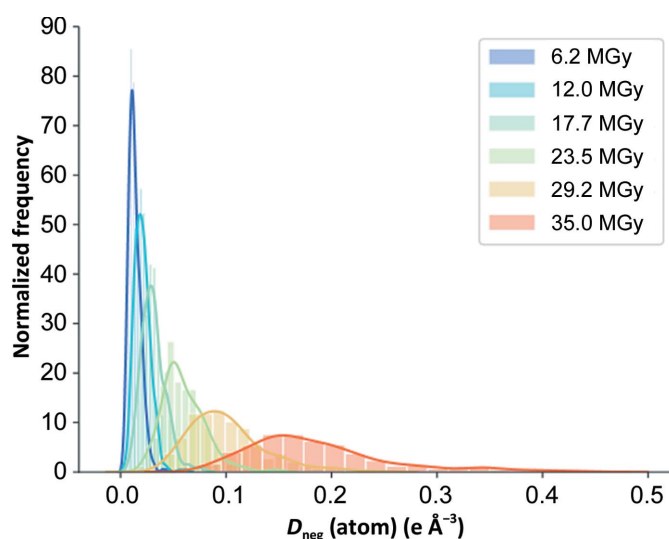
Figure 9
Histogram of $D_{neg}(atom)$ for data sets 7, 13, 19, 15, 31 and 37.
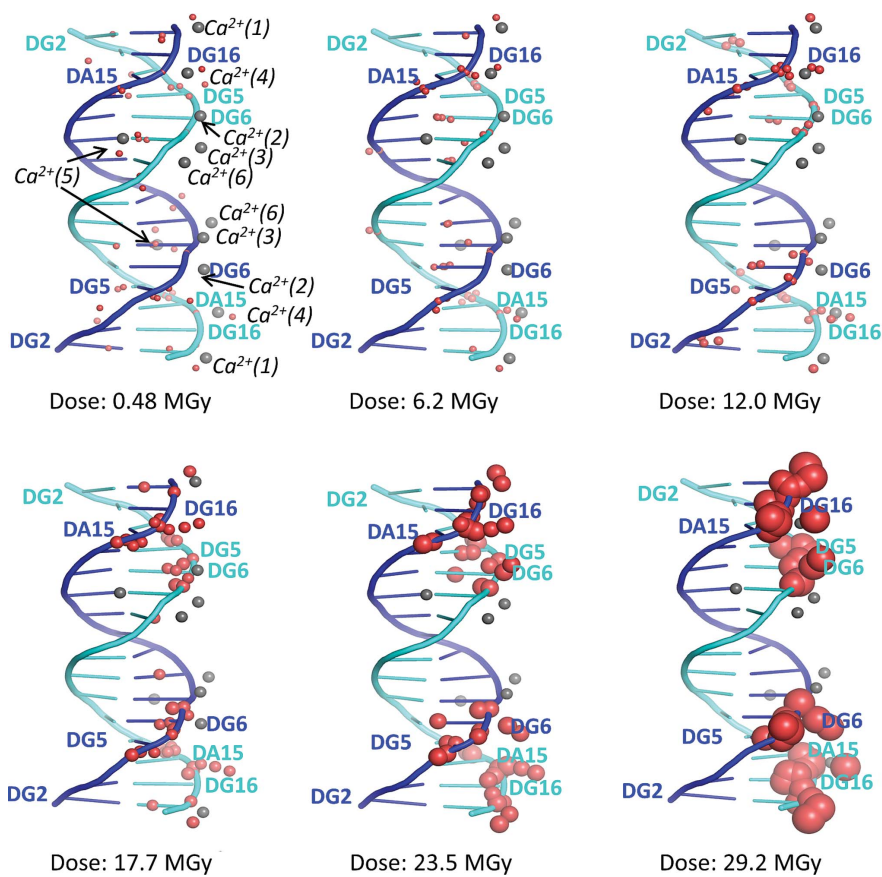
Figure 10
Representation of the top 25 specific damage sites on each of the two DNA strands (50 in total) at different doses. Specific damage sites are represented as red spheres, with radii proportional to the electron-density loss. (Ca^{2+} ions are shown as grey spheres and the nucleotide residues that are most affected, as well as the first residue G2, are labelled.)

Figure 11
DNA damage of nucleotides, including base–sugar bond, sugar–phosphate bond and water–phosphate bond loss. D_{neg}(atom) values are shown for the top ten radiation-damage sites. [See Figs. 1(b) and 10 for the locations of these sites in the DNA chains.]

The average atomic B factors for the seven refined structures were analysed and were normalized to the value for the structure derived from data set $n = 1$ (Supplementary Fig. S3). They showed a linear increase with dose with a gradient of 0.007 MGy^{-1}, which can be compared with values of 0.0041 MGy^{-1} for both DNA strands in the bacterial protein–DNA complex (C.Esp1396I–DNA; Bury *et al.*, 2015).

4. Discussion

This radiation-damage study at 100 K on a crystal of a DNA 16-mer diffracting to 1.8 Å resolution showed that, for this example, DNA alone is somewhat more robust to global radiation damage than the lysozyme used here as a control and which was irradiated under the same beam conditions. This conclusion comes with the proviso that any scavenging capacity of cryo-buffers *etc.* was comparable. The $D_{1/2}$ for the 1.8 Å resolution DNA 16-mer crystal data was 18.9 ($\pm$2.6) MGy (an average for all six series of eight data sets each $\pm$ standard deviation) compared with 9 MGy for the lysozyme control for 1.4 Å resolution data. There are various $D_{1/2}$ values in the literature for native lysozyme crystals (no explicit scavengers added) examined at 100 K, among them being two studies on several crystals each: 17 MGy for all data to 1.6 Å (Teng & Moffat, 2002), and 12.5–12.9 MGy for all resolution shells to 1.7 Å (de la Mora *et al.*, 2011). These values were obtained using rather different dose estimation methods, but both indicate the comparative radiation sensitivity of lysozyme. In comparison, the $D_{1/2}$ for the C.Esp1396I protein–DNA complex was 43 MGy (DWD) for all data to 2.8 Å resolution; see the supporting information of Bury *et al.* (2015); the same value was obtained for all data to 2.2 Å resolution for holoferritin and apoferritin using a beam with a top-hat profile bigger than the crystal giving homogeneous irradiation (Owen *et al.*, 2006).

We have also demonstrated that for the DNA 16-mer crystal the relative isotropic B factor, B_{rel}, varies very linearly with increasing dose over the whole of the reported dose range (Fig. 5) without a plateau at high doses as has been observed for some protein crystals [see, for example, Fig. 1(*d*) in Garman (2010)]. The coefficient of sensitivity (Kmetko *et al.*, 2006), $s_{AD} = \Delta B_{rel}/8\pi^2\Delta D$, is 0.014 Å^2 MGy^{-1}, which is similar to the average value of 0.012 Å^2 MGy^{-1} determined for four protein crystals at 100 K (lysozyme, thaumatin, catalase and apoferritin; Kmetko *et al.*, 2006), indicating that according to this metric the DNA in the crystal suffers comparable rates of damage to that of protein crystals.

residue types were at a dose of about 10 MGy (Bury *et al.*, 2015). For the current DNA 16-mer crystal, we observed very similar resistance: the normalized frequency of DNA nucleotides involved in specific radiation damage reaches 0.2 at 35.0 MGy.

The unit-cell volume expansion noted for the DNA crystal here is in the same range as is observed for proteins (Fig. 5), being about 1.5% for 30 MGy. However, for crystals of the same protein it shows great variability, but for instance has been reported to be around 2% in crystals of holoferritin at a dose of 30 MGy (Garman, 2010).

The average atomic B factors of the refined models of the DNA 16-mer increase from 49 to 58 Å^2 over the dose range studied, a gradient of 0.29 $\text{Å}^2 \text{ MGy}^{-1}$ (8.4 Å^2 in 28.7 MGy), which if normalized to the average B factor for the lowest-dose data set gives a change with dose of 0.007 MGy^{-1} (see Supplementary Fig. S1). In the C.Esp1396I protein–DNA complex study (Bury $et\ al.$, 2015), the normalized (to unity for the lowest dose) atomic B-factor DNA gradient was 0.004 MGy^{-1} compared with the gradient for the protein of around 0.006 MGy^{-1}, which is very close to that found here for the DNA alone. In that work, thymine was reported to be slightly more damaged than the other bases, with guanine being the least affected, in contrast to the finding here of preferential damage to guanine in the crystal of DNA alone. As already mentioned, the results of Bury and coworkers showed that the onset of specific damage is at significantly higher doses for DNA than for protein within the C.Esp1396I protein–DNA complex, and that when it does occur specific damage is more evenly distributed between the four base types than it is amongst the protein residues.

Using the innovative, highly streamlined and automated $RIDL$ pipeline for the identification of X-ray-induced structural damage patterns, we have established the existence of differential specific damage rates with respect to dose at 100 K in a DNA 16-mer crystal. The $RIDL$ tool removed the requirement for manual inspection of $F_{\text{obs},n} - F_{\text{obs},1}$ maps and outputs metrics that have been explicitly designed to objectively characterize site-specific radiation damage to atoms (Bury, McGeehan $et\ al.$, 2016).

The site-specific damage to the DNA 16-mer studied here is primarily located on the phosphates. The chemical nature and mechanism of this 'phosphate' damage was not investigated in this study, but we hypothesize that it involves P—O and/or O–sugar bond breakage. Indeed, sophisticated electronic structure calculations have suggested a mechanism by which the latter linkage, in particular, may be broken by low-energy electrons (Simons, 2007). Increased phosphate freedom can produce a displacement, and thus lead to changes in negative density in OMIT maps. This phosphate displacement could also explain the loss of density around one of the phosphate O atoms at high doses. We note that owing to the greater X-ray cross-section of the DNA compared with the 41% solvent by volume, more ionizations will occur in the DNA than in its surroundings. The sensitivity of the structure to specific radiation damage was lowest in the region of the aromatic groups of the nucleobases and highest at the phosphate moieties. As noted above, guanine was the most damaged base, presumably acting as a hole trap owing to its relatively low ionization potential (Jovanovic & Simic, 1986; Becker $et\ al.$, 2007).

Using a metric calculated by $RIDL$ and comparing segments coordinating and lacking calcium ions, we showed that the occurrence of electron-density loss is highest in the vicinity of certain calcium ions in the structure. Since only some of these ions are damaged, this is clearly not a direct effect of the larger X-ray photon-absorption cross-section of these heavy ions. Furthermore, as there are calcium-complexed and noncomplexed DNA segments in the structure, the radiation sensitivity of these could be directly compared.

The results of this experiment suggested that, interestingly, the differential sensitivity to damage among the various phosphates as detailed in the results was far greater than that observed among disulfide bonds in protein crystals [for example, for lysozyme all four disulfide bonds show damage by a dose of 0.14 MGy, as shown in Fig. 6 of Sutton $et\ al.$ (2013)]. The fact that we observed differential damage to the phosphates presumably indicates again that the damage was not solely direct.

The radiation tolerance of DNA crystals should be investigated further by pursuing experiments focused on a range of crystals containing DNA segments of different lengths, and if possible in the absence of bound heavy atoms. It would be particularly interesting to study DNA in complex with the radiosensitizing drug cisplatin, since its synergistic effects are used extensively to enhance the effects of radiotherapy for cancer treatment [see, for example, Marcu $et\ al.$ (2003) and Fayette $et\ al.$ (2015) for a review, and Fayette $et\ al.$ (2015) for a treatment-regime comparison] and the underlying mechanisms of this are poorly understood.

References

Alizadeh, E., Orlando, T. M. & Sanche, L. (2015). $Annu.\ Rev.\ Phys.\ Chem.$ **66**, 379–398.
Alizadeh, E. & Sanche, L. (2014). $Eur.\ Phys.\ J.\ D$, **68**, 97.

Becker, D., Adhikary, A. & Sevilla, M. D. (2007). *Charge Migration in DNA: Perspectives from Physics, Chemistry, and Biology*, edited by T. Chakraborty, pp. 139–175. Berlin, Heidelberg: Springer.

Becker, D. & Sevilla, M. D. (1993). *DNA and Chromatin Damage Caused by Radiation*, edited by J. T. Lett & W. K. Sinclair, pp. 121–180. San Diego: Academic Press.

Berman, H. M., Westbrook, J., Feng, Z., Gilliland, G., Bhat, T. N., Weissig, H., Shindyalov, I. N. & Bourne, P. E. (2000). *Nucleic Acids Res.* **28**, 235–242.

Boudaïffa, B., Cloutier, P., Hunting, D., Huels, M. A. & Sanche, L. (2000). *Science*, **287**, 1658–1660.

Brockhauser, S., Di Michiel, M., McGeehan, J. E., McCarthy, A. A. & Ravelli, R. B. G. (2008). *J. Appl. Cryst.* **41**, 1057–1066.

Burmeister, W. P. (2000). *Acta Cryst.* D**56**, 328–341.

Bury, C., Garman, E. F., Ginn, H. M., Ravelli, R. B. G., Carmichael, I., Kneale, G. & McGeehan, J. E. (2015). *J. Synchrotron Rad.* **22**, 213–224.

Bury, C. S., Carmichael, I. & Garman, E. F. (2017). *J. Synchrotron Rad.* **24**, 7–18.

Bury, C. S., Carmichael, I., McGeehan, J. E. & Garman, E. F. (2016). *Radiat. Phys. Chem.* **128**, 118–125.

Bury, C. S. & Garman, E. F. (2018). *J. Appl. Cryst.* **51**, 952–962.

Bury, C. S., McGeehan, J. E., Antson, A. A., Carmichael, I., Gerstel, M., Shevtsov, M. B. & Garman, E. F. (2016). *Acta Cryst.* D**72**, 648–657.

Cadet, J., Delatour, T., Douki, T., Gasparutto, D., Pouget, J.-P., Ravanat, J.-L. & Sauvaigo, S. (1999). *Mutat. Res.* **424**, 9–21.

De la Mora, E., Carmichael, I. & Garman, E. F. (2011). *J. Synchrotron Rad.* **18**, 346–357.

Emsley, P., Lohkamp, B., Scott, W. G. & Cowtan, K. (2010). *Acta Cryst.* D**66**, 486–501.

Evans, P. (2006). *Acta Cryst.* D**62**, 72–82.

Evans, P. R. & Murshudov, G. N. (2013). *Acta Cryst.* D**69**, 1204–1214.

Fayette, J., Molin, Y., Lavergne, E., Montbarbon, X., Racadot, S., Poupart, M., Ramade, A., Zrounba, P., Céruse, P. & Pommier, P. (2015). *Drug. Des. Dev. Ther.* **9**, 6203–6210.

Garman, E. F. (2010). *Acta Cryst.* D**66**, 339–351.

Garman, E. F. & Owen, R. L. (2006). *Acta Cryst.* D**62**, 32–47.

Garman, E. F. & Weik, M. (2017). *Methods Mol. Biol.* **1607**, 467–490.

Halliwell, B. & Gutteridge, J. M. C. (1998). *Free Radicals in Biology and Medicine*, 3rd ed. Oxford University Press.

Helliwell, J. R. (1988). *J. Cryst. Growth*, **90**, 259–272.

Holton, J. M. (2009). *J. Synchrotron Rad.* **16**, 133–142.

Howells, M. R., Beetz, T., Chapman, H. N., Cui, C., Holton, J. M., Jacobsen, C. J., Kirz, J., Lima, E., Marchesini, S., Miao, H., Sayre, D. S., Shapiro, D. A., Spence, J. H. C. & Starodub, D. (2009). *J. Electron Spectrosc. Relat. Phenom.* **170**, 4–12.

Huang, D. B., Phelps, C. B., Fusco, A. J. & Ghosh, G. (2005). *J. Mol. Biol.* **346**, 147–160.

Jovanovic, S. V. & Simic, M. G. (1986). *J. Phys. Chem.* **90**, 974–978.

Kadhim, M. A., Hill, M. A. & Moore, S. R. (2006). *Radiat. Prot. Dosimetry*, **122**, 221–227.

Kempner, E. S. (1993). *Q. Rev. Biophys.* **26**, 27–48.

Kmetko, J., Husseini, N. S., Naides, M., Kalinin, Y. & Thorne, R. E. (2006). *Acta Cryst.* D**62**, 1030–1038.

Marcu, L., van Doorn, T. & Olver, I. (2003). *Acta Oncol.* **42**, 315–325.

Matsui, Y., Sakai, K., Murakami, M., Shiro, Y., Adachi, S., Okumura, H. & Kouyama, T. (2002). *J. Mol. Biol.* **324**, 469–481.

McCoy, A. J., Grosse-Kunstleve, R. W., Adams, P. D., Winn, M. D., Storoni, L. C. & Read, R. J. (2007). *J. Appl. Cryst.* **40**, 658–674.

McGeehan, J. E., Carpentier, P., Royant, A., Bourgeois, D. & Ravelli, R. B. G. (2007). *J. Synchrotron Rad.* **14**, 99–108.

Michael, B. D. & O'Neill, P. (2000). *Science*, **287**, 1603–1604.

Murshudov, G. N., Skubák, P., Lebedev, A. A., Pannu, N. S., Steiner, R. A., Nicholls, R. A., Winn, M. D., Long, F. & Vagin, A. A. (2011). *Acta Cryst.* D**67**, 355–367.

Nave, C. & Garman, E. F. (2005). *J. Synchrotron Rad.* **12**, 257–260.

O'Neill, P., Stevens, D. L. & Garman, E. (2002). *J. Synchrotron Rad.* **9**, 329–332.

Owen, R. L., Axford, D., Nettleship, J. E., Owens, R. J., Robinson, J. I., Morgan, A. W., Doré, A. S., Lebon, G., Tate, C. G., Fry, E. E., Ren, J., Stuart, D. I. & Evans, G. (2012). *Acta Cryst.* D**68**, 810–818.

Owen, R. L., Holton, J. M., Schulze-Briese, C. & Garman, E. F. (2009). *J. Synchrotron Rad.* **16**, 143–151.

Owen, R. L., Rudiño-Piñera, E. & Garman, E. F. (2006). *Proc. Natl Acad. Sci. USA*, **103**, 4912–4917.

Potterton, L., Agirre, J., Ballard, C., Cowtan, K., Dodson, E., Evans, P. R., Jenkins, H. T., Keegan, R., Krissinel, E., Stevenson, K., Lebedev, A., McNicholas, S. J., Nicholls, R. A., Noble, M., Pannu, N. S., Roth, C., Sheldrick, G., Skubak, P., Turkenburg, J., Uski, V., von Delft, F., Waterman, D., Wilson, K., Winn, M. & Wojdyr, M. (2018). *Acta Cryst.* D**74**, 68–84.

Ptasińska, S. & Sanche, L. (2007). *Phys. Rev. E*, **75**, 031915.

Ravelli, R. B. G. & Garman, E. F. (2006). *Curr. Opin. Struct. Biol.* **16**, 624–629.

Ravelli, R. B. G. & McSweeney, S. M. (2000). *Structure*, **8**, 315–328.

Sauter, N. K., Hattne, J., Grosse-Kunstleve, R. W. & Echols, N. (2013). *Acta Cryst.* D**69**, 1274–1282.

Simons, J. (2007). *Adv. Quantum Chem.* **56**, 171–188.

Snell, E. H., Bellamy, H. D., Rosenbaum, G. & van der Woerd, M. J. (2007). *J. Synchrotron Rad.* **14**, 109–115.

Spotheim-Maurizot, M. & Davídková, M. (2011). *Mutat. Res.* **711**, 41–48.

Sutton, K. A., Black, P. J., Mercer, K. R., Garman, E. F., Owen, R. L., Snell, E. H. & Bernhard, W. A. (2013). *Acta Cryst.* D**69**, 2381–2394.

Swarts, S. G., Gilbert, D. C., Sharma, K. K., Razskazovskiy, Y., Purkayastha, S., Naumenko, K. A. & Bernhard, W. A. (2007). *Radiat. Res.* **168**, 367–381.

Taberman, H., Bury, C. S., van der Woerd, M. J., Snell, E. H. & Garman, E. F. (2019). *J. Synchrotron Rad.* **26**, 931–944.

Teng, T. & Moffat, K. (2000). *J. Synchrotron Rad.* **7**, 313–317.

Teng, T.-Y. & Moffat, K. (2002). *J. Synchrotron Rad.* **9**, 198–201.

Warren, A. J., Axford, D. & Owen, R. L. (2019). *J. Synchrotron Rad.* **26**, 991–997.

Weik, M., Ravelli, R. B. G., Kryger, G., McSweeney, S., Raves, M. L., Harel, M., Gros, P., Silman, I., Kroon, J. & Sussman, J. L. (2000). *Proc. Natl Acad. Sci. USA*, **97**, 623–628.

Winn, M. D., Ballard, C. C., Cowtan, K. D., Dodson, E. J., Emsley, P., Evans, P. R., Keegan, R. M., Krissinel, E. B., Leslie, A. G. W., McCoy, A., McNicholas, S. J., Murshudov, G. N., Pannu, N. S., Potterton, E. A., Powell, H. R., Read, R. J., Vagin, A. & Wilson, K. S. (2011). *Acta Cryst.* D**67**, 235–242.

Winter, G., Waterman, D. G., Parkhurst, J. M., Brewster, A. S., Gildea, R. J., Gerstel, M., Fuentes-Montero, L., Vollmar, M., Michels-Clark, T., Young, I. D., Sauter, N. K. & Evans, G. (2018). *Acta Cryst.* D**74**, 85–97.

Yokoya, A., Cunniffe, S. M. T. & O'Neill, P. J. (2002). *J. Am. Chem. Soc.* **124**, 8859–8866.

Zeldin, O. B., Brockhauser, S., Bremridge, J., Holton, J. M. & Garman, E. F. (2013). *Proc. Natl Acad. Sci. USA*, **110**, 20551–20556.

Zeldin, O. B., Gerstel, M. & Garman, E. F. (2013). *J. Appl. Cryst.* **46**, 1225–1230.